J. Plasma Phys. (2021), *vol*. 87, 905870402 © The Author(s), 2021.
Published by Cambridge University Press
doi:10.1017/S0022377821000684

A numerical study of gravity-driven instability in strongly coupled dusty plasma. Part 2. Hetero-interactions between a rising bubble and a falling droplet

Vikram S. Dharodi †,‡

Mechanical Engineering, Michigan State University, East Lansing, MI 48824, USA

(Received 10 March 2021; revised 15 June 2021; accepted 15 June 2021)

In part 1 (V. S. Dharodi and A. Das, J. Plasma Phys. 87 (02), 905870216 (2021)), we simulated the individual dynamics of a bubble (a localized low-density region) and a droplet (a localized high-density region) in a strongly coupled dusty plasma. We observed that under the influence of gravity, the result of a pair of counter-rotating vorticity lobes causes the bubble to rise and droplet to fall. With an interest to understand the hetero-(bubble–droplet) interactions between them, we extend this study to their combined evolution through the following two arrangements. First, both are placed side-by-side in a row at the same height. We observe that the overall dynamics is governed by the competition between the net vertical motion induced by gravity and rotational motion induced by the pairing between two co-rotating inner vorticity lobes. In the second arrangement, the vertically aligned bubble (below) and droplet (above) after collision exchange their partners and subsequently start to move horizontally in opposite directions away from each other. This horizontal movement becomes slower with increasing coupling strength. For these arrangements, we consider varying the distance between the fixed-size bubble and droplet, and varying the coupling strength. To visualize the bubble–droplet interactions, a series of two-dimensional simulations have been conducted in the framework of an incompressible generalized hydrodynamic viscoelastic fluid model.

Key words: dusty plasmas, strongly coupled plasmas, complex plasmas

1. Introduction

Rayleigh–Taylor (RT) instability occurs when an external force like gravity accelerates a heavy fluid into a lighter one (Rayleigh 1900; Taylor 1950; Chandrasekhar 1981). Apart from RT instability, buoyancy-driven (BD) instability is another form of gravity-driven instability which is also associated with the density fluctuations in a medium. We have introduced the BD situation by including a bubble as a localized low-density region and a droplet as a localized high-density region compared with the fluid in which they are placed. The BD instability determines whether an object sinks or floats in the fluid in which it is immersed. Under the influence of gravity, a bubble has a tendency to float

† Email address for correspondence: dharodiv@msu.edu
‡ Present address: Institute for Plasma Research, HBNI, Bhat, Gandhinagar 382 428, India.

upwards while a droplet sinks against the surrounding fluid. Bubbles and droplets have been studied separately (for example, see Shew & Pinton 2006; Gaudron, Warnez & Johnsen 2015; Dollet, Marmottant & Garbin 2019 for bubbles and Dwyer 1989; Cristini & Tan 2004; Zhu, Sui & Djilali 2008; Leong & Le 2020 for drops) and both together (Mokhtarzadeh-Dehghan & El-Shirbini 1985; Chen *et al.* 2008; Tabor *et al.* 2011). An understanding of the interaction of gas bubbles and liquid droplets with themselves or with particles or with a colloid probe is desired for a wide range of applications, which include the manufacturing of cosmetics and pharmaceuticals, oil recovery (Zhao *et al.* 2017), printing and deinking, emulsion stability (Xie *et al.* 2017), foodstuffs such as ice cream and mousse (Van Aken 2001), and in mineral flotation (Liu *et al.* 2002; Niewiadomski *et al.* 2007). Recently, detailed experiments (Kong *et al.* 2019) and numerical simulations (Zhang, Chen & Ni 2019) have been conducted to investigate the interactions between a pair of bubbles rising side by side. Additionally, both homo- (bubble–bubble and drop–drop) and hetero- (bubble–drop) interactions between air bubbles and oil droplets have been measured using atomic force microscopy by Tabor *et al.* (2011). In the context of a plasma medium, studies of bubbles and/or droplets under various conditions have been carried out (Stenzel & Urrutia 2012; Arzhannikov *et al.* 2013; Wang *et al.* 2015; Ning *et al.* 2021). In a dusty plasma laboratory, the density fluctuations related to the bubble and/or droplet are mainly induced by laser pulses. Experimentally, the dynamics of bubbles has been studied by Chu *et al.* (2003) and Teng *et al.* (2008). Chen, Chu & Lin (2006) investigated bubble–bubble interactions. The spontaneous formation of bubbles, drops and spraying cusps under the influence of thermophoresis has been reported by Schwabe *et al.* (2009).

In part 1 of this investigation, we separately explored the dynamics of a bubble and a droplet in the incompressible limit of strongly coupled dusty plasmas (SCDPs). We observed that a falling droplet process is equivalent to a rising bubble because both had symmetry in the spatial distribution. We described the SCDP using an incompressible generalized hydrodynamic (i-GHD) fluid model (Kaw & Sen 1998; Kaw 2001). This model treats SCDP as a viscoelastic (VE) fluid that characterizes the viscoelastic effects through two coupling parameters: shear viscosity η and the Maxwell relaxation parameter τ_m (Frenkel 1955). We observed that the rising of a bubble and falling of a droplet become weaker with increasing coupling strength (ratio η/τ_m), which represents the viscoelastic behaviour of the medium. In the present paper, to investigate the nature of interactions between a bubble and a droplet, we have both together in the same fluid within the framework of the i-GHD fluid model. We consider two arrangements: First, the droplet and bubble are placed side by side in a row at the same height; Second, the bubble and droplet are aligned in a column where the droplet is placed above the bubble. For these arrangements, we consider varying the distance between the fixed-size bubble and droplet, and varying the coupling strength which represents the viscoelastic nature of the medium. To the best of our knowledge, the bubble–droplet interactions have been observed for the first time in dusty plasmas, thus an experimental research effort is desirable to validate this work.

This paper is organized in the following sections. In § 2, the basic model equations are described and then are re-written in § 2.1 as a set of coupled equations for the implementation of our numerical scheme. In § 3, to report the simulation results, first we develop some qualitative understanding by using the model equations through schematic diagrams for the considered bubble–droplet density profiles. For horizontally placed blobs, the simulations are performed for three initial spacings: widely spaced ($d \gg 2a_c$), medium spaced ($d > 2a_c$) and closely spaced ($d \approx 2a_c$), where a_c is the core radius. Next, the droplet is placed above the bubble in a vertical column with a fixed initial spacing. The role

https://doi.org/10.1017/S0022377821000684 Published online by Cambridge University Press

of coupling strength on the bubble–droplet density dynamics is depicted in the form of transverse shear (TS) waves through the respective vorticity contour plots. To develop a better physical insight into the dynamics of each phenomenon, the inviscid limit of hydrodynamic (HD) fluids is also simulated for each case. Finally, in § 4, we conclude the paper with a summary.

2. The numerical model and simulation methodology

The generalized hydrodynamic fluid model supports both the incompressible transverse and compressible longitudinal modes. To study only the effect of transverse modes on the bubble–droplet interaction and to avoid the coupling with the longitudinal mode, we consider the incompressible limit of dusty plasmas. In the incompressible limit, the Poisson equation is replaced by the quasineutrality condition and charge density fluctuations are ignored. The dust fluid flow under gravity acceleration $\boldsymbol{g}$ is characterized by a coupled set of continuity and momentum equations:

$$\frac{\partial \rho_d}{\partial t} + \boldsymbol{\nabla} \cdot (\rho_d \boldsymbol{v}_d) = 0, \tag{2.1}$$

$$\left[1 + \tau_m \left(\frac{\partial}{\partial t} + \boldsymbol{v}_d \cdot \boldsymbol{\nabla}\right)\right] \left[\rho_d \left(\frac{\partial \boldsymbol{v}_d}{\partial t} + \boldsymbol{v}_d \cdot \boldsymbol{\nabla} \boldsymbol{v}_d\right) + \rho_d \boldsymbol{g} + \rho_c \boldsymbol{\nabla} \phi_d\right] = \eta \nabla^2 \boldsymbol{v}_d, \tag{2.2}$$

respectively, and the incompressible condition is given as

$$\boldsymbol{\nabla} \cdot \boldsymbol{v}_d = 0. \tag{2.3}$$

The derivation of these normalized equations has been discussed in detail in our earlier papers (Dharodi, Tiwari & Das 2014; Dharodi *et al.* 2016) along with the procedure of its numerical implementation and validation. Here, $\rho_d = n_d m_d$ is the mass density of the dust fluid, where n_d is the number density of the dust fluid which is normalized by its equilibrium value n_{d0} and m_d is the mass of the dust particle. The dust charge density $\rho_c = n_d Z_d$, Z_d is the charge on each dust grain with no consideration of charge fluctuation. The dust charge potential ϕ_d is normalized by $K_B T_i/e$. The parameters e, T_i and K_B are the electronic charge, ion temperature and Boltzmann constant, respectively. The time, length and dust fluid velocity $\boldsymbol{v}_d$ are normalized by the inverse of the dust plasma frequency $\omega_{pd}^{-1} = (4\pi (Z_d e)^2 n_{d0}/m_{d0})^{-1/2}$, plasma Debye length $\lambda_d = (K_B T_i/4\pi Z_d n_{d0} e^2)^{1/2}$ and $\lambda_d \omega_{pd}$, respectively. In the HD limit i.e. τ_m=0, this model represents a simple hydrodynamic fluid through the Navier–Stokes equation.

2.1. *Simulation methodology*

For the numerical modelling the above generalized momentum equation (2.2) is transformed into a set of two coupled equations,

$$\rho_d \left(\frac{\partial \boldsymbol{v}_d}{\partial t} + \boldsymbol{v}_d \cdot \boldsymbol{\nabla} \boldsymbol{v}_d\right) + \rho_d \boldsymbol{g} + \rho_c \boldsymbol{\nabla} \phi_d = \boldsymbol{\psi}, \tag{2.4}$$

$$\frac{\partial \boldsymbol{\psi}}{\partial t} + \boldsymbol{v}_d \cdot \boldsymbol{\nabla} \boldsymbol{\psi} = \frac{\eta}{\tau_m} \nabla^2 \boldsymbol{v}_d - \frac{\boldsymbol{\psi}}{\tau_m}. \tag{2.5}$$

https://doi.org/10.1017/S0022377821000684 Published online by Cambridge University Press

We consider a two-dimensional (2-D) system that lies in the xy plane, where the x-coordinate is in the horizontal and the y is in the vertical. Thus the above variables depend on x and y, i.e. $\boldsymbol{\psi}(x, y)$, $\boldsymbol{v}_d(x, y)$ and $\rho_d(x, y)$. The quantity $\boldsymbol{\psi}(x, y)$ is the strain produced in the elastic medium by the time-varying velocity fields. The density gradient and potential gradient are taken along the y-axis i.e. $\partial\rho_d/\partial y$ and $\partial\phi_d/\partial y$, respectively. The acceleration $\boldsymbol{g}$ is applied opposite to the fluid density gradient i.e. $-g\hat{y}$. We also assume no initial flow i.e. $\boldsymbol{v}_{d0} = 0$ at $t = 0$. With small perturbations; density, scalar potential and dust velocity can be written as

$$\rho_d(x, y, t) = \rho_{d0}(y, t = 0) + \rho_{d1}(x, y, t), \tag{2.6}$$

$$\phi_d(x, y, t) = \phi_{d0}(y, t = 0) + \phi_{d1}(x, y, t), \tag{2.7}$$

$$\boldsymbol{v}_d(x, y, t) = 0 + \boldsymbol{v}_{d1}(x, y, t), \tag{2.8}$$

respectively. We then re-write (2.4) under the equilibrium condition, $\rho_{d0}g = -\rho_c\partial\phi_{d0}/\partial y$ and using the above relations (2.6), (2.7) and (2.8).

$$\frac{\partial \boldsymbol{v}_d}{\partial t} + \boldsymbol{v}_d\cdot\nabla\boldsymbol{v}_d + \frac{\rho_{d1}}{\rho_d}\boldsymbol{g} + \frac{\rho_c}{\rho_d}\nabla\phi_{d1} = \frac{\boldsymbol{\psi}}{\rho_d}. \tag{2.9}$$

By taking the curl of (2.9) and using the Boussinesq approximation ($\rho_{d0} \gg \rho_{d1}$), the contribution from $\nabla\phi_{d1}$ becomes zero i.e. $\nabla \times \nabla\phi_{d1} = 0$, and we get

$$\frac{\partial \xi_z}{\partial t} + (\boldsymbol{v}_d \cdot \nabla)\xi_z = \frac{1}{\rho_{d0}}\nabla \times \rho_{d1}\boldsymbol{g} + \nabla \times \frac{\boldsymbol{\psi}}{\rho_d}. \tag{2.10}$$

Here, $\xi_z(x, y) = \nabla \times \boldsymbol{v}_d(x, y)$ is the vorticity, which is normalized by the dust plasma frequency. The final numerical model equations in terms of variables x and y become

$$\frac{\partial \rho_d}{\partial t} + (\boldsymbol{v}_d \cdot \nabla)\rho_d = 0, \tag{2.11}$$

$$\frac{\partial \boldsymbol{\psi}}{\partial t} + (\boldsymbol{v}_d \cdot \nabla)\boldsymbol{\psi} = \frac{\eta}{\tau_m}\nabla^2\boldsymbol{v}_d - \frac{\boldsymbol{\psi}}{\tau_m}, \tag{2.12}$$

$$\frac{\partial \xi_z}{\partial t} + (\boldsymbol{v}_d \cdot \nabla)\xi_z = -\frac{g}{\rho_{d0}}\frac{\partial \rho_{d1}}{\partial x} + \frac{\partial}{\partial x}\left(\frac{\psi_y}{\rho_d}\right) - \frac{\partial}{\partial y}\left(\frac{\psi_x}{\rho_d}\right). \tag{2.13}$$

We use the LCPFCT package (Boris *et al.* 1993) to numerically solve the above set of coupled nonlinear equations (2.11), (2.12) and (2.13). This package is based on the finite difference scheme associated with the flux-corrected algorithm. The velocity at each time step is updated by using the velocity–vorticity relation $\nabla^2\boldsymbol{v}_d = -\nabla \times \boldsymbol{\xi}$. This velocity–vorticity relation has been solved by using the FISPACK package (Swarztrauber, Sweet & Adams 1999). Both packages are FORTRAN subprograms. Throughout the simulation studies, boundary conditions are periodic in the horizontal direction (x-axis) and non-periodic along the vertical (y-axis) direction where the effects of perturbed quantities die out before hitting the boundary of the simulation box. In each case, a grid convergence study has been carried out to ensure the grid independence of the numerical results.

In the HD limit i.e. τ_m=0, (2.12) has singularity. To avoid this singularity, we put $\tau_m = 0$ in the generalized momentum equation (2.2) and then by taking the curl, under the same

https://doi.org/10.1017/S0022377821000684 Published online by Cambridge University Press

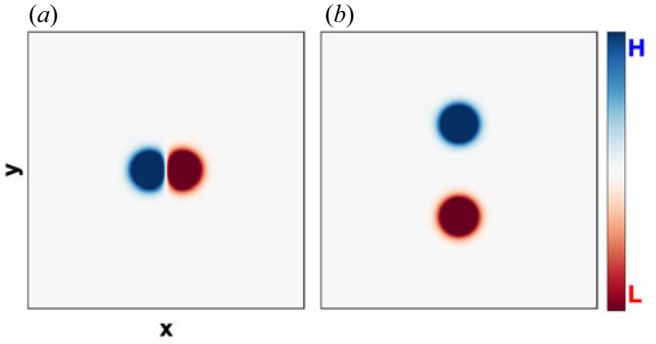

FIGURE 1. The initial density profiles at time $t = 0$: (*a*) the droplet (left) and the bubble (right) are placed at the same height, and (*b*) the droplet and the bubble are aligned vertically with the droplet placed above the bubble. In the colourbar, letter ***H*** is the acronym of the high-density region and ***L*** stands for the low-density region.

above considered conditions and assumptions, one gets the HD vorticity equation:

$$\frac{\partial \xi_z}{\partial t} + (\boldsymbol{v}_d \cdot \boldsymbol{\nabla})\xi_z = -\frac{g}{\rho_{d0}}\frac{\partial \rho_{d1}}{\partial x} + \eta \nabla^2 \xi_z. \tag{2.14}$$

Thus, for pure HD cases ($\tau_m = 0$) we numerically solve the set of (2.11) and (2.14), where the dust fluid velocity at each time step is updated by using the above velocity–vorticity relation. It should be noted that the density evolution has been discussed in terms of blob/blobs while vorticity evolution in terms of lobe/lobes.

3. Simulation results

To understand the bubble–droplet dynamics, we consider the two arrangements shown in figure 1: Arrangement (A) in figure 1(*a*), the droplet (left) and bubble (right) are placed in a row at the same height; Arrangement (B) in figure 1(*b*), the bubble (bottom) and droplet (top) are aligned in a column. For both arrangements, the total density is $\rho_d = \rho_{d0} + \rho_{d1}$, where ρ_{d0} is the background density and the net density inhomogeneity is given by

$$\rho_{d1} = \rho'_{d1} + \rho'_{d2}. \tag{3.1}$$

The Gaussian density inhomogeneity of the droplet centred at (x_{c1}, y_{c1}), with radius a_{c1}, is

$$\rho'_{d1} = \rho'_{01}\exp\left(\frac{-(x - x_{c1})^2 - (y - y_{c1})^2}{a_{c1}^2}\right), \tag{3.2}$$

and the Gaussian density inhomogeneity of the bubble centred at (x_{c2}, y_{c2}), with radius a_{c2}, is

$$\rho'_{d2} = -\rho'_{02}\exp\left(\frac{-(x - x_{c2})^2 - (y - y_{c2})^2}{a_{c2}^2}\right). \tag{3.3}$$

Throughout the entire numerical simulations, $g = 10$, $\rho_{d0} = 5$, $\rho'_{01} = \rho'_{02} = 0.5$ and $a_{c1} = a_{c2} = 2.0$ are held constant. Thus, both the bubble and droplet have spatial symmetry and spaced by distance $d = \sqrt{(x_{c2} - x_{c1})^2 + (y_{c2} - y_{c1})^2}$.

https://doi.org/10.1017/S0022377821000684 Published online by Cambridge University Press

It would be good to develop some basic qualitative understanding about the bubble–droplet evolution before reporting the simulation results. For an inviscid flow ($\eta = \tau_m = 0$), the vorticity equation (2.14) using (3.1), (3.2) and (3.3) becomes

$$\frac{\partial \xi_z}{\partial t} + (\boldsymbol{v}_d \cdot \nabla)\xi_z = \frac{2g}{\rho_{d0}}(x - x_{c1})\rho'_{d1} - \frac{2g}{\rho_{d0}}(x - x_{c2})\rho'_{d2}. \tag{3.4}$$

Here, the right-hand side represents the net vorticity of the combined bubble and droplet arrangement. Under the influence of gravity, both terms depict the oppositely propagating dipolar vorticities each having a pair of counter-rotating (or unlike-sign) lobes. The first term acts like a buoyant force on the droplet and causes a vertical downward motion, while the second acts like a buoyant force on the bubble and results in a vertical upward motion (Dharodi & Das 2021).

For the arrangement (A), using the right-hand side of (3.4), figure 2(*b*) represents the schematic images of vorticities, which correspond to the bubble–droplet density profiles in figure 2(*a*). The curved solid arrows over the lobes represent their direction of rotation while the net propagation is indicated by the vertical and curved dotted arrows. In these schematic images, the spacing '*d*' between a droplet and a bubble decreases from left to right. From the figure it is observed that the overall dynamics is governed by the competition between the rotational motions induced by the pairing between two co-rotating inner vorticity lobes and the net vertical motion of two dipolar vorticities (downward for the droplet and upward for the bubble) induced by gravity. To understand this, first, let us discuss the case if the bubble and droplet are widely spaced (left of panel *a*), the counter-rotating vorticity lobes related to the droplet (left of panel *b*) cause a vertical downward motion (indicated by the vertical downward dotted arrow) while those related to the bubble cause a vertical upward motion for the bubble (indicated by vertical upward dotted arrow). Owing to large distance '*d*', there is almost no interaction between the rising bubble and falling droplet, so their dynamics would be mainly governed by gravity i.e. the same as the individual cases. However, by decreasing the separation distance (see the remaining panels from left to right) enhances the possibility of vorticity pairing through the co-rotating inner lobes. This pairing leads to the merging process (Von Hardenberg *et al.* 2000; Meunier, Le Dizès & Leweke 2005; Josserand & Rossi 2007) which results in the rotation (counterclockwise) of the entire structure about a common centre of rotation. Thus, this rotational effect is found to be proportional to the pairing of the vorticity lobes. It is noted that, because we have the droplet on the left and the bubble on the right, the net vorticity would rotate counterclockwise and *vice versa*. For arrangement (B), the droplet is aligned above the bubble in a vertical column, as shown in figure 1(*b*). As discussed above, the generated dipolar vorticity related to the bubble causes a vertical upward motion but a vertical downward motion for the droplet. Thus, as time progresses, the two oppositely propagating dipolar vorticities collide with each other and then exchange their partners which results in two new dipolar structures that propagate away from each other in an orthogonal direction to the initial propagation.

Thus far, under the influence of gravity, the merging of two co-rotating vortices and convection of dipolar vorticity (two counter-rotating vortices) are the two major transport phenomena. The above discussed dynamics is particularly true for an inviscid fluid where no dissipation or source terms exist. The vorticity equation (2.10) or (2.13) for VE fluids in addition to the gravity term includes an additional term $\nabla \times (\boldsymbol{\psi}/\rho_d)$ on the right-hand side. This term incorporates the TS waves emerging from the rotating lobes into the medium (Dharodi *et al.* 2014, 2016). The speed of these waves ($\sqrt{\eta/\tau_m}$) is proportional to the coupling strength (η/τ_m) of the medium. For a fixed d, the effect of the VE nature on

https://doi.org/10.1017/S0022377821000684 Published online by Cambridge University Press

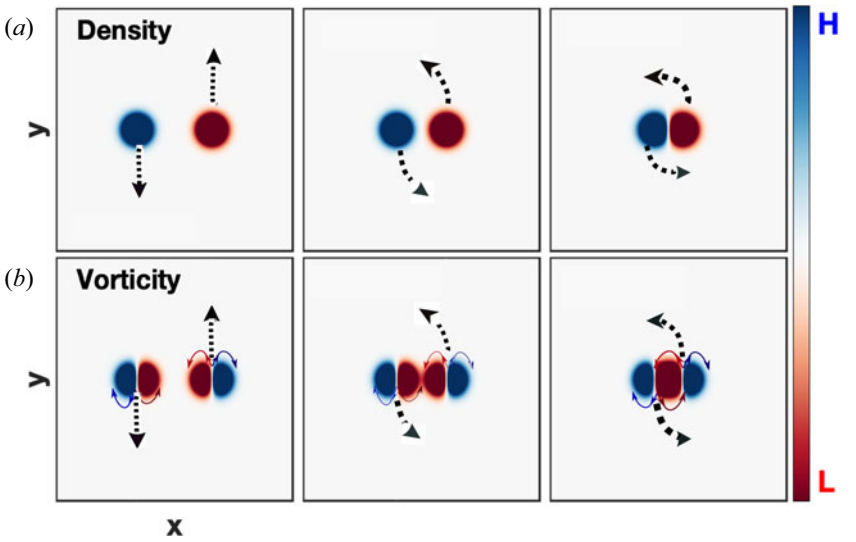

FIGURE 2. A schematic diagram of a droplet and a bubble placed in a row at the same height. The spacing between them decreases from left to right: (*a*) the density profile; and (*b*) the vorticity. The net propagation is indicated by the dotted arrows in (*a*,*b*) and the curved solid arrows represent the direction of rotation of the lobes in (*b*).

the bubble–droplet interactions has been introduced through varying the coupling strength of the medium. The bubble–droplet dynamics will be visualized through the numerical simulations in detail in the subsequent sections.

3.1. *Aligned horizontally*

We consider a system of length $lx = ly = 24\pi$ units with 512×512 grid points in both the x and y directions. The system along the x-axis and y-axis is from -12π to 12π units. The droplet and bubble are placed at the same height $(y_{c1}, y_{c2}) = (0, 0)$. It is worth noting at this point that the interaction between a bubble and a droplet depends, apart from the nature of the medium, on their sizes i.e. a_{c1}/a_{c2} (both have equal and fixed, $a_c = a_{c1} = a_{c2} = 2.0$), on their shapes (both are symmetric) and on the initial spacing between them $d = x_{c2} - x_{c1}$. Here, the simulations are performed for three spacings: widely spaced ($d \gg 2a_c$), medium spaced ($d > 2a_c$) and closely spaced ($d \approx 2a_c$). The separation distances are $d = 12$ with $(x_{c1}, x_{c2}) = (6.0, -6.0)$, $d = 8$ with $(x_{c1}, x_{c2}) = (4.0, -4.0)$, and $d = 4.4$ with $(x_{c1}, x_{c2}) = (2.2, -2.2)$, for cases (i), (ii) and (iii), respectively. In each case, the coupling strength has been introduced as the mild-strong ($\eta = 2.5$, $\tau_m = 20$), medium-strong ($\eta = 2.5$, $\tau_m = 10$) and strong or strongest ($\eta = 2.5$, $\tau_m = 5$), as well as pure viscosity ($\eta = 2.5$, $\tau_m = 0$).

3.1.1. *Case (i): Widely spaced* ($d \gg 2a_c$)

Initially, the droplet ($x_{c1} = -6.0$) and bubble ($x_{c2} = 6.0$) are quite well-spaced ($d = 12 \gg 2a_c, a_c = 2$) without any overlap between the inner lobes of the vorticities. First, let us understand the bubble–droplet dynamics for an inviscid fluid. Here, the absence of any dissipative and source terms makes this combined evolution like an individual one. In part I (Dharodi & Das 2021) of this investigation, we studied a rising bubble and a falling droplet separately. We observed the falling droplet process is equivalent to the rising bubble as they initially have axisymmetry in their density profiles. Owing to gravity,

https://doi.org/10.1017/S0022377821000684 Published online by Cambridge University Press

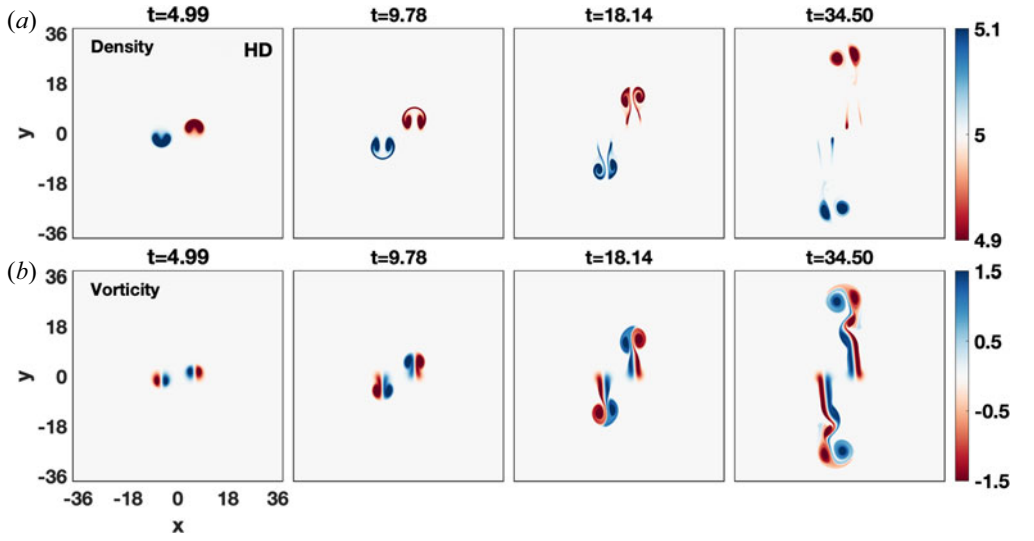

FIGURE 3. Time evolution of bubble–droplet density (a) and vorticity (b) for an inviscid fluid. Both are separated by distance $d = 12$ units ($d \gg 2a_c$). The dynamics of the rising bubble and falling droplet are almost independent and evolve the same as the individual ones.

the initially circular density blobs change into crescent shapes. As time progresses, both the bubble and droplet blobs break up into two distinct density blobs. The two blobs of the bubble/droplet propagate upward/downward as a single entity leaving behind a wake-like structure in the background fluid. Such observations are clearly evident from the time evolution of the bubble–droplet density profile in figure 3(a). The reason for the rising/falling bubble/droplet can be understood from the vorticity evolution in figure 3(b). In figure 3(b), as the simulation begins, the buoyant forces are induced in the form of two oppositely propagating dipolar vorticities each having two counter-rotating lobes. The result is the vertical upward motion for the bubble, which appears to be independent to the vertically downward motion of the droplet, as discussed in detail above.

Next, it would be interesting to see the bubble–droplet dynamics in SCDPs that are depicted as VE fluids. The SCDPs, in addition to the forward motion, favour the radial emission of TS waves into the ambient fluid from each rotating vorticity lobe. These waves have the same symmetry of a lobe, and their speed is proportional to the coupling strength (η/τ_m) of the medium (Dharodi *et al.* 2014, 2016). In other words, a medium with stronger coupling strength would support the faster TS waves. The faster wave travels a greater distance in the same amount of time and that results in a faster spreading of the lobes. Thus, for the current horizontal arrangement, a medium with stronger coupling strength shows a higher probability of vorticity interaction or pairing between two like-sign inner lobes at an earlier time, which in turn would enhance the rotational effect in the medium. In addition, the emerging TS waves from both the outermost lobes also help to enhance this interaction by pushing the inner lobes towards each other. All this suggests that the competition between the rotational strength of two inner like-sign vorticity lobes arising from the lateral interaction and forward vertical motion of two dipolar vorticities (unlike-sign lobes) owing to the gravity governs the net dynamics. In the subsequent cases, only the coupling strength is changing through the elastic term τ_m for the fixed viscosity $\eta = 2.5$.

https://doi.org/10.1017/S0022377821000684 Published online by Cambridge University Press

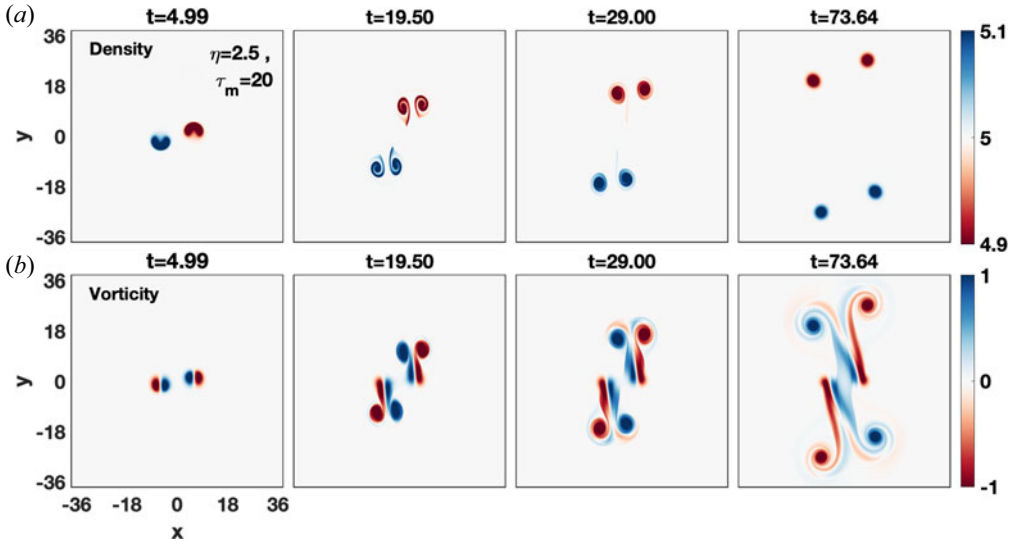

FIGURE 4. Time evolution of bubble–droplet density (*a*) and vorticity (*b*) for a viscoelastic fluid with $\eta = 2.5$ and $\tau_m = 20$. In comparison to the HD fluid (figure 3), there is a decrease in the rising/falling rate of the bubble/droplet and an increase in the horizontal separation between the lobes.

Let us start with the mild-strong case i.e. $\eta = 2.5$, $\tau_m = 20$ which is shown in figure 4. Similar to figure 3, here also the forward vertical motion arising from gravity dominates over the lateral interaction. However, in addition, it is evident from figure 4(*b*) that there is an emission of TS waves surrounding each of the vorticity lobes and no such waves exist in figure 3(*b*). These waves cause the mutual pushing between unlike-sign lobes which in turn enhance the separation between them with time. In addition to the lobes separation, the TS wave reduces the strength of dipoles thereby reducing their propagation. The relative observations of figures 4(*a*) and 3(*a*) clearly reflect the aforementioned fact. Next, figure 5 shows the evolution of density (*a*) and vorticity (*b*) for the medium-strong coupling strength $\eta = 2.5$, $\tau_m = 10$. Also in figure 5(*b*), the forward vertical motion dominates over the lateral interaction. However, owing to the higher coupling strength, the reduction in forward motion and enlargement in the horizontal separation between the unlike-sign dipoles are higher compared with the earlier case (figure 4; $\eta = 2.5$, $\tau_m = 20$).

A VE fluid with a stronger coupling strength ($\eta = 2.5$, $\tau_m = 5.0$) than the earlier cases is shown in figure 6. This would support an even faster speed of the TS waves. Therefore, this, in addition to slowing down the forward motion of lobes, will enhance the vorticity exchange between the inner lobes at an earlier time. From figure 6(*b*), it is clearly evident that the rotation between inner lobes owing to the merging process dominates over the forward vertical motion. As time passes, the combined effect of motion under gravity and the pairing of inner lobes causes the continuous stretching and spreading of the inner lobes (see the second and third vorticity column). These inner lobes rotate around each other for a while and merge into an elliptic vortex at later times (fourth vorticity column). Here, because of the emission of TS waves, the rotating elliptic vortex grows in time and merging occurs without the need of a third vortex (Kevlahan & Farge 1997). The outer two lobes are gradually wrapped around the rotating elliptic vortex. This results in a confined persistently rotating structure around a common centre. See the supplementary material and movies available at https://doi.org/10.1017/S0022377821000684.

https://doi.org/10.1017/S0022377821000684 Published online by Cambridge University Press

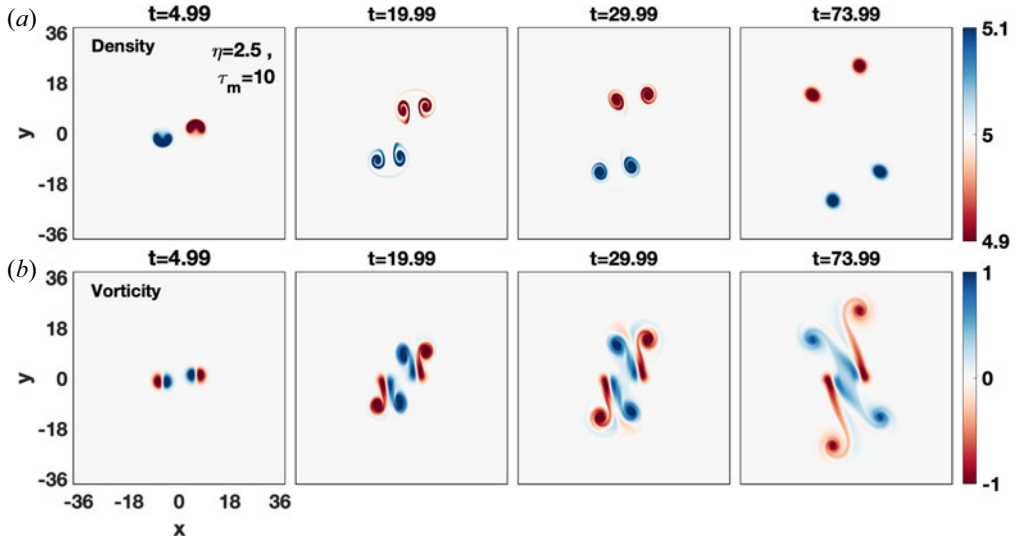

FIGURE 5. Time evolution of bubble–droplet density (a) and vorticity (b) for a viscoelastic fluid with $\eta = 2.5$ and $\tau_m = 10$. Both the density blobs are separated by distance $d = 12$ units ($d \gg 2a_c$, $a_c = 2$).

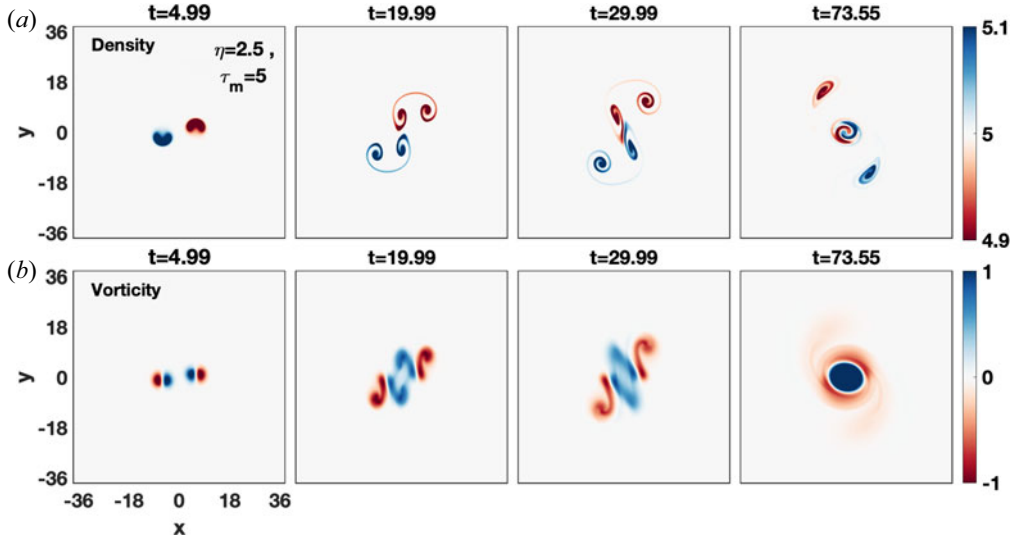

FIGURE 6. Time evolution of bubble–droplet density (a) and vorticity (b) for a viscoelastic fluid with $\eta = 2.5$ and $\tau_m = 5$. Both the density blobs are separated by distance $d = 12$ units ($d \gg 2a_c$, $a_c = 2$). The rotation between inner lobes owing to the merging process dominates over the forward vertical motion.

In figure 6(a), the initially circular density blobs change into crescent shapes. Owing to the reduction in the vertical forward motion and enhancement in the transverse direction, these crescent shapes get wider in the horizontal direction for a while and then transform into curved structures with dumbbell-shaped edges (see the second density panel) unlike in an inviscid fluid (figure 3a). Later, the merging/pairing between two inner blobs of different densities form a centre vortex and separates it from two outer blobs (one from a

https://doi.org/10.1017/S0022377821000684 Published online by Cambridge University Press

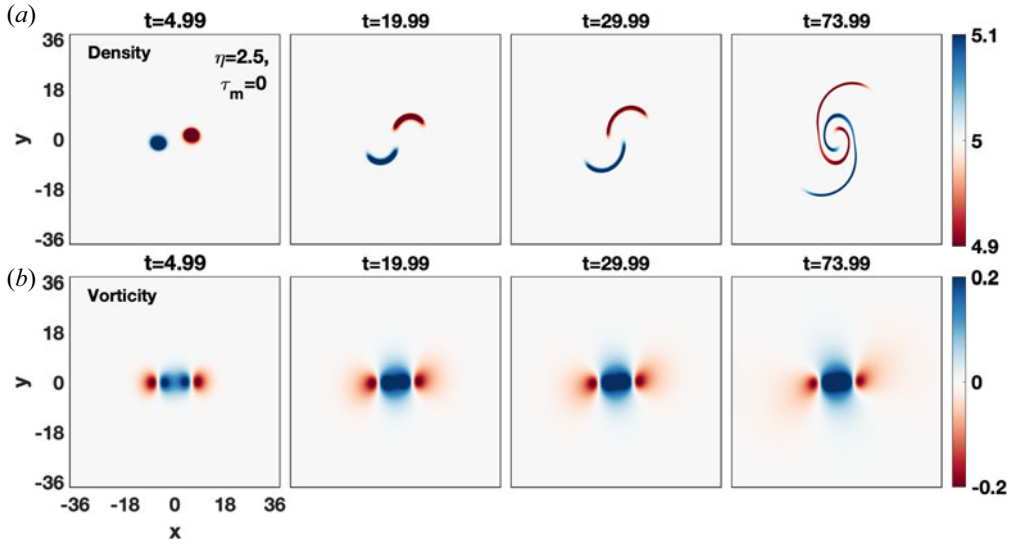

FIGURE 7. Time evolution of bubble–droplet density (*a*) and vorticity (*b*) for pure viscous HD fluid ($\eta = 2.5$; $\tau_m = 0$). Here, owing to the viscous damping force, in the presence of gravity, the density crescent structures are transformed into spirals with time.

bubble and one from a droplet). All this results in a tripolar structure (see the third density panel) with two outer blobs revolving around the centre vortex like satellites. Finally, the fourth density panel has a centre vortex with two rolling distinct density arms and both the outer blobs spiral into one arm. This observation favours our recent study of spiral waves in density heterogeneous VE fluids where the number of spiral arms is proportional to the number of different densities that coexist (Dharodi 2020). This tripole is symmetric as it does not move but merely rotates (van Heijst, Kloosterziel & Williams 1991). In the supplement we include a movie to accompany the static images shown in figure 6.

To determine the pure viscous effect of viscosity on bubble–droplet dynamics, we also simulated a pure viscous HD fluid (see the density evolution in figure 7 for $\eta = 2.5$; $\tau_m = 0$) by using (2.11) and (2.14). In figure 7(*b*) the viscous effect is so strong over the gravity effect that there is almost no forward vertical motion. The vorticity lobes spreading owing to viscosity enhance the pairing between the like-sign inner lobes with time (Huang 2005) and this, in turn, induces a regularly rotating flow at the centre. This reduction in the vertical motion and strong rotating flow at the centre transforms the crescent density blobs into two persistently rotating spirals with time, as shown in figure 7(*a*). Again, this observation confirms that the number of spiral arms is proportional to the number of different densities that coexist (Dharodi 2020).

Thus, the bubble–droplet dynamics are significantly affected by the presence of τ_m which controls the viscous spreading of vorticity lobes through the existence of the transverse mode in SCDPs.

3.1.2. *Case (ii): Medium spaced* ($d > 2a_c$)

At the start, the droplet ($x_{c1} = -4.0$) and bubble ($x_{c2} = 4.0$) are medium spaced ($d = 8$), two inner lobes of vorticities just touch each other. Here, the spacing is less than the earlier widely spaced case ($d = 12$). Thus, there should be a higher probability of interaction between a bubble and a droplet. Figure 8 displays the time evolution of the density (*a*) and vorticity (*b*) profiles for an inviscid fluid. In the beginning, figure 8 shows

https://doi.org/10.1017/S0022377821000684 Published online by Cambridge University Press

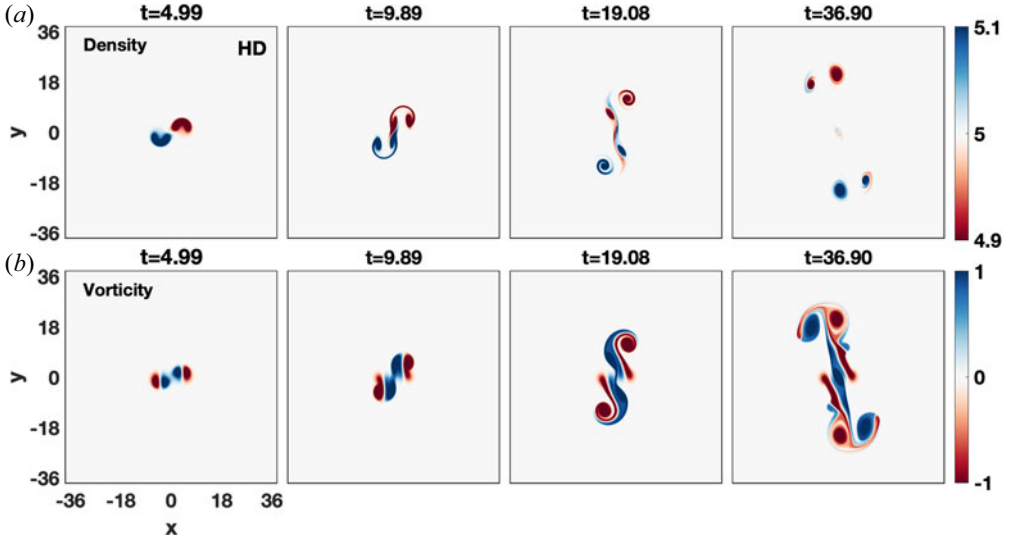

FIGURE 8. Time evolution of bubble–droplet density (*a*) and vorticity (*b*) for an inviscid fluid. Initially, the droplet and bubble have a small overlapping between the inner lobes. Both have some interactions in the beginning but later start to evolve independently as separate ones with some diversion from the vertical direction in comparison to the widely spaced HD case shown in figure 3.

a small side-by-side overlapping between the inner lobes owing to some closeness between them. Later, the forward motion (induced by gravity) of a bubble and a droplet dominates over this transverse overlapping and results in them evolving independently as separate ones with some diversion from the vertical direction compared with the earlier widely spaced inviscid case (figure 3).

To visualize the effect of coupling strength, we start with the mild-strong coupling case; $\eta = 2.5$, $\tau_m = 20$ in figure 9. In figure 9(*a*,*b*) the merging process dominates over the forward vertical motion and this results in the formation of a tripolar structure. For the earlier widely spaced case ($d = 12$) the tripolar structure formed only for a strong coupling strength ($\eta = 2.5$; $\tau_m = 5$). Thus, the decreasing distance increases the pairing between the bubble and droplet. Next, for the medium-strong case $\eta = 2.5$; $\tau_m = 10$ in figure 10(*a*,*b*), the formation of a tripolar structure takes place earlier compared with the earlier case ($\eta = 2.5$, $\tau_m = 20$). This tripolar structure has a smaller size and high rotation speed. The smaller size means less area of convection of the fluid across the medium. The rotating outer density blobs are also no longer circular. For the case of strong coupling strength $\eta = 2.5$; $\tau_m = 5.0$, figure 11, the reduction in vertical motion is higher and the net structure rapidly merges into a tripolar. As time passes, the outer vorticity lobe arms are spread out around the inner rotating elliptical vortex and smoothed out by the emerging TS shear waves. Thus, more axial symmetric and confined structure formation takes place.

A comparative analysis of all the above cases shows that the confinement of the vortex structures is proportional to the increasing coupling strength. Figure 12 shows the evolution of the bubble–droplet density of a pure viscous fluid with $\eta = 2.5$; $\tau_m = 0$. Under the influence of gravity, in the absence of the TS wave, the crescent structures transform into two regularly rotating spirals. These spirals are elongated vertically owing to the gravitational force. The comparison of figures 12 and 7(*a*) shows that the medium

https://doi.org/10.1017/S0022377821000684 Published online by Cambridge University Press

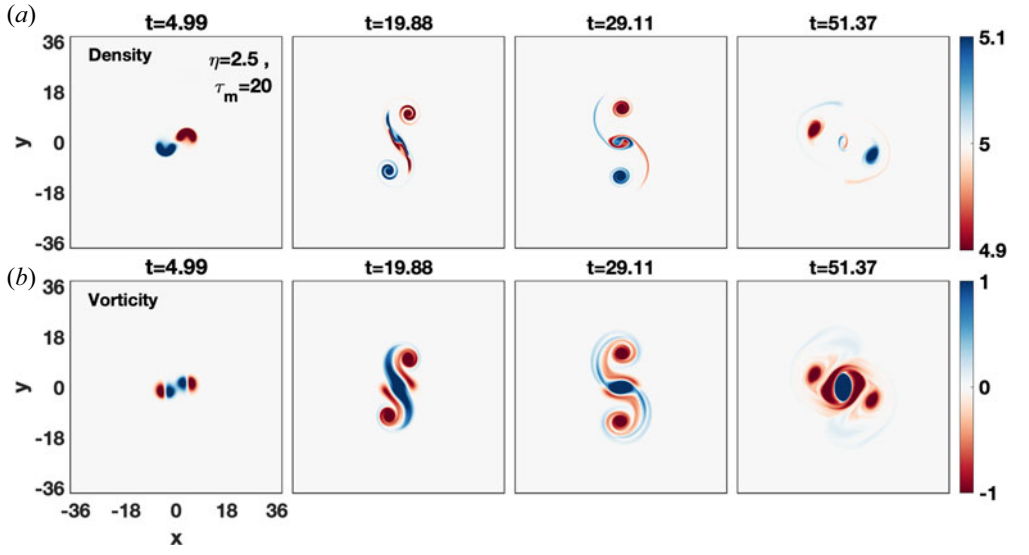

FIGURE 9. Time evolution of bubble–droplet density (*a*) and vorticity (*b*) for a viscoelastic fluid with $\eta = 2.5$ and $\tau_m = 20$. Both are separated by distance $d = 8.0$ units ($d > 2a_c$, $a_c = 2$).

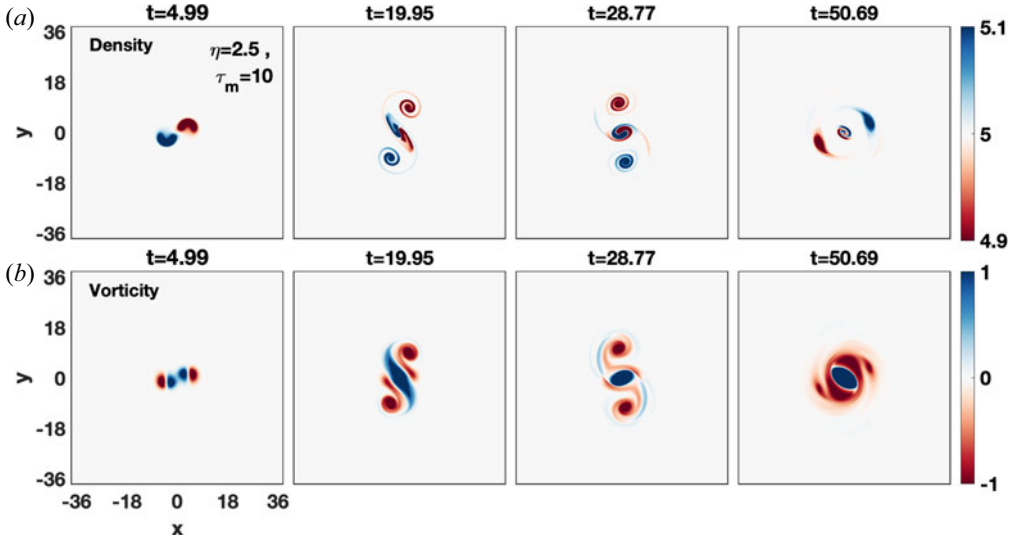

FIGURE 10. Time evolution of bubble–droplet density (*a*) and vorticity (*b*) for a viscoelastic fluid with $\eta = 2.5$ and $\tau_m = 10$.

spaced blobs ($d > 2a_c$) show a higher rotation rate of spirals than widely spaced blobs ($d \gg 2a_c$).

3.1.3. *Case (iii): Closely spaced* ($d \approx 2a_c$)

To begin with, the droplet ($x_{c1} = -2.2$) and bubble ($x_{c2} = 2.2$) are placed close enough ($d = 4.4 \approx 2a_c$) so that both the like-sign inner lobes of vorticity almost overlap with each other to yield a tripolar vorticity structure. As the simulation begins, the overlapped centre vortex starts to rotate counterclockwise and this results in the rotation of whole

https://doi.org/10.1017/S0022377821000684 Published online by Cambridge University Press

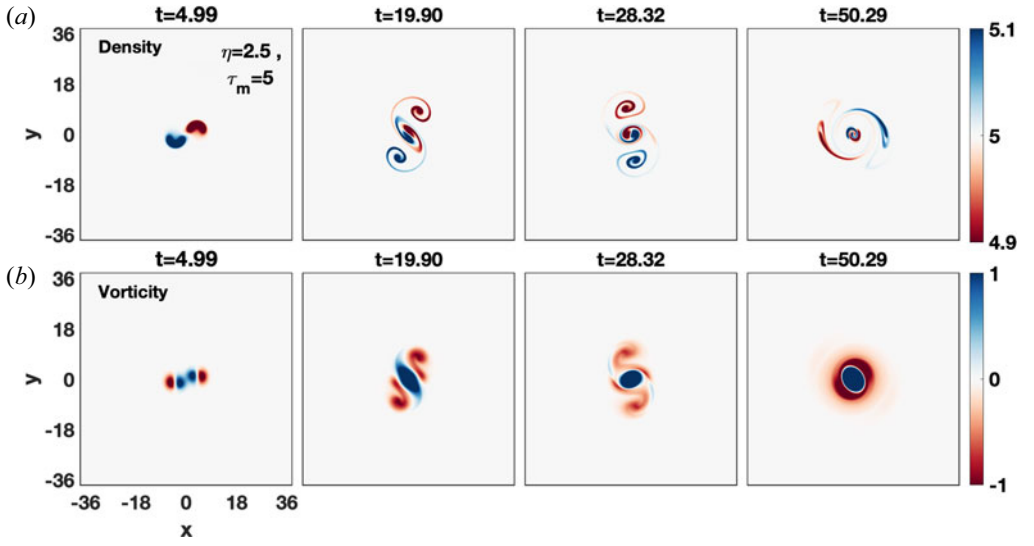

FIGURE 11. Time evolution of bubble–droplet density (a) and vorticity (b) for a viscoelastic fluid with $\eta = 2.5$ and $\tau_m = 5$. Both are separated by distance $d = 8.0$ units ($d > 2a_c$, $a_c = 2$).

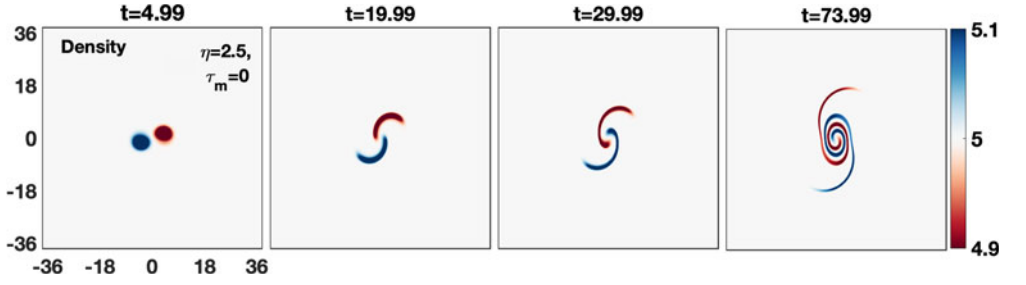

FIGURE 12. Time evolution of bubble–droplet density (a) and vorticity (b) for pure viscous HD fluid ($\eta = 2.5$; $\tau_m = 0$). The medium spaced blobs ($d > 2a_c$) show a higher rotation rate of spirals than those of the widely spaced case $d \gg 2a_c$ (figure 7).

structure about a common centre even for an inviscid fluid, as shown in figure 13. This rotating flow transforms the crescent-shaped density blobs into thin intertwining spirals as shown in figure 14. Up to $t \approx 15$, there is no significant difference in density profiles for the simple fluid and VE cases. These common evolution features can be clearly seen up to the second column of figures 15(a), 15(b), and 15(c) for varying relaxation parameters $\tau_m = 20$, 10 and 5, respectively; for the fixed viscosity $\eta = 2.5$. At a later stage, the density configuration evolves quite differently for the inviscid fluid and VE fluid. In the case of the inviscid fluid we observe two constantly rotating prominent crescent structures along with faint spirals. However, in the VE fluid, the crescent structures and the spirals get mixed owing to the emerging TS wave (see figure in the supplemental material). This results in the absence of crescent structures and the whole structure evolves into spirals outward away from the centre of rotation. Comparison of the last two columns from figure 15(a) ($\eta = 2.5$; $\tau_m = 20$), figure 15(b) ($\eta = 2.5$; $\tau_m = 10$) and figure 15(c) ($\eta = 2.5$; $\tau_m = 5$) clearly confirms the earlier statement that the stronger coupling strength leads to a more axial symmetric and confined structure formation. Again, for the viscous fluid, owing to

https://doi.org/10.1017/S0022377821000684 Published online by Cambridge University Press

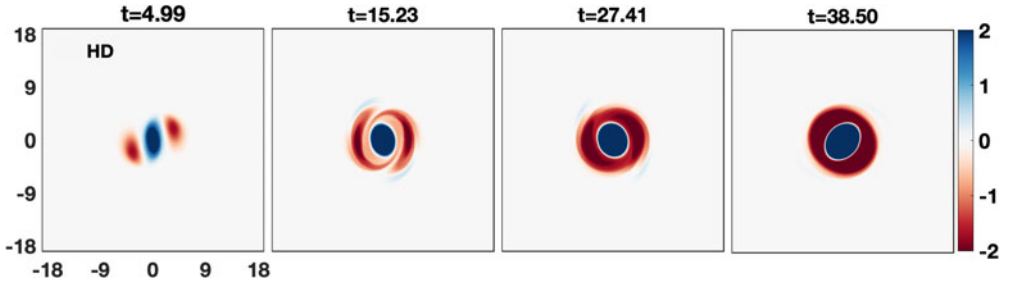

FIGURE 13. Time evolution of bubble–droplet vorticity for an inviscid fluid corresponding to figure 14.

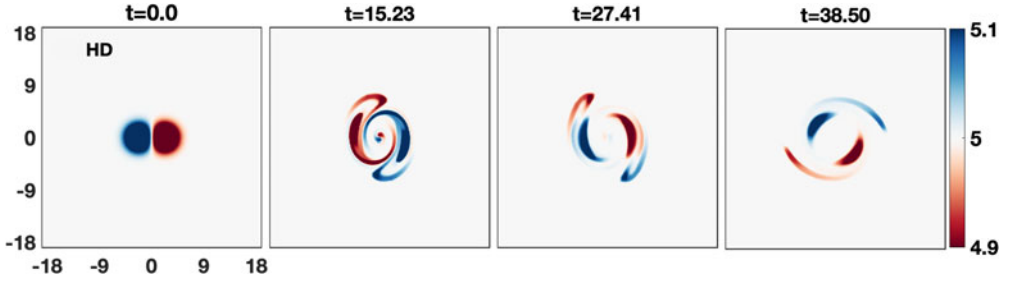

FIGURE 14. Time evolution of bubble–droplet density for an inviscid fluid. Both are separated by distance $d = 4.4$ units ($d \approx 2a_c$, $a_c = 2$).

the closeness,figure 16 shows a higher rotation rate of spirals compared with the medium spaced (figure 12*a*) blobs.

3.2. *Aligned vertically*

We now consider the second arrangement (B) where the droplet is placed above the bubble in a vertical column (see figure 1*b*). Here, the coupling strength (η/τ_m) is the only varying parameter. We have a system of length $lx = ly = 12\pi$ units with 512×512 grid points in both the x and y directions. The system along the x-axis and y-axis are from -6π to 6π units. For this case the values of the parameters a_c, x_c, y_c, ρ' for the droplet and bubble are 2.0, 0.0, 4π, 0.5 and 2.0, 0.0, -4π, 0.5, respectively. For this configuration in contrast to the previous case in figure 1(*a*), there is no rotation of density blobs. Here, the falling droplet and rising bubble simply collide with each other during the course of evolution. Figure 17(*a*) displays the evolution of this density configuration for the inviscid fluid. It is evident from the figure that as these two structures evolve, they hit each other and their blobs become separated. One blob from the bubble and one blob from the droplet get paired with each other and subsequently move horizontally. Figure 18(*a*) shows the evolution of the same density configuration for a VE fluid ($\eta = 2.5$; $\tau_m = 20$). It is evident from the figure that compared with the inviscid fluid, the horizontal propagation of the structures is slower and vertical separation between density blobs is larger with time. This horizontal reduction and vertical separation further increase with increasing coupling strength, as shown in figure 19(*a*) ($\eta = 2.5$; $\tau_m = 5$). Such dynamics can be understood in terms of TS waves from the relative observations of figures 18(*b*) and 19(*b*).

We know from the above discussion that a stronger coupling strength of a medium induces faster TS waves. The faster TS waves result in a larger mutual pushing between

https://doi.org/10.1017/S0022377821000684 Published online by Cambridge University Press

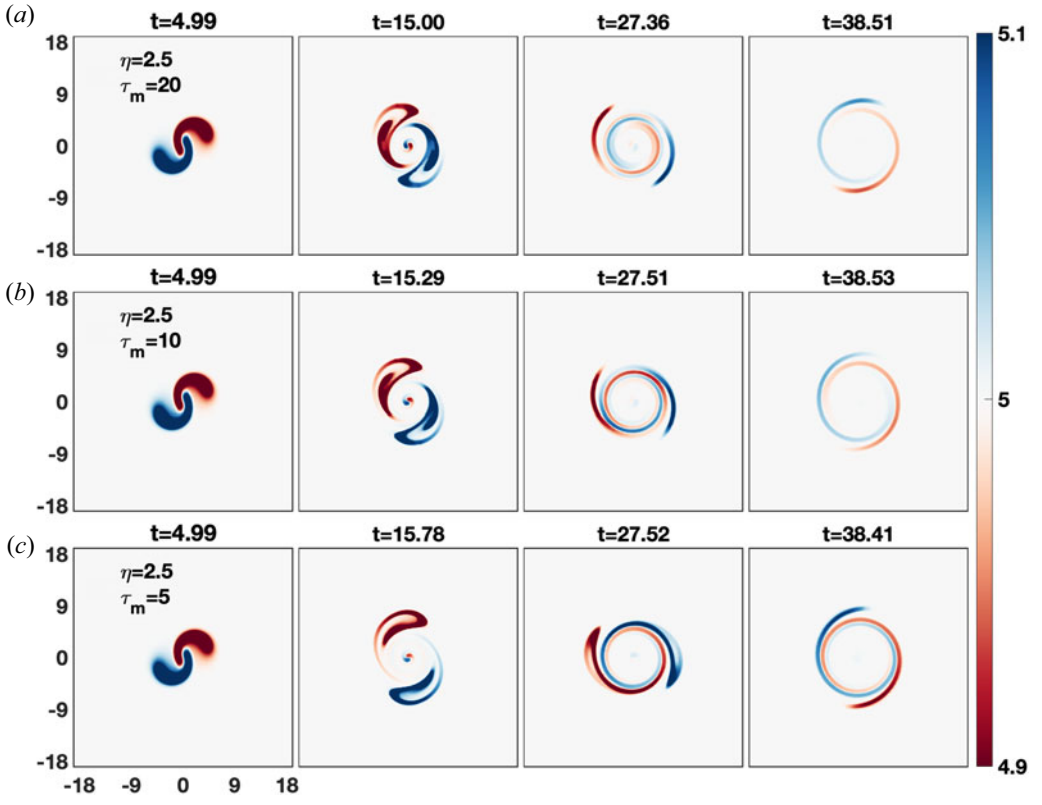

FIGURE 15. Time evolution of bubble–droplet density in viscoelastic fluids for fixed viscous term $\eta = 2.5$; and varying coupling strength arising from changing relaxation parameter $\tau_m =$ 20, 10 and 5 in (*a*), (*b*) and (*c*), respectively. See supplemental material for the vorticity profiles corresponding to these density profiles.

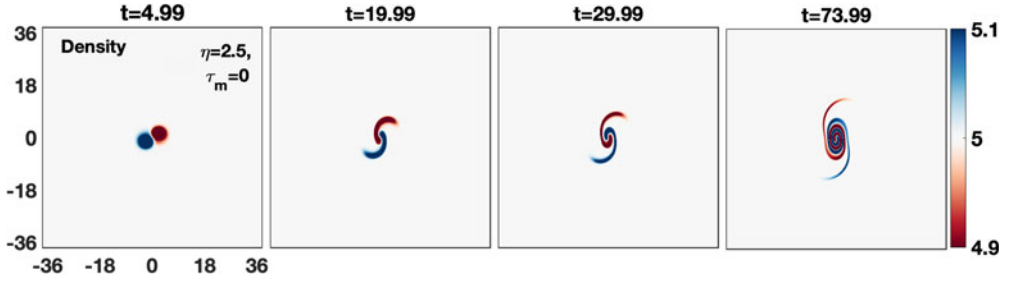

FIGURE 16. Time evolution of bubble–droplet density (*a*) and vorticity (*b*) for pure viscous HD fluid ($\eta = 2.5$; $\tau_m = 0$). The closely spaced blobs ($d \approx 2a_c$) show a higher rotation rate of spirals than the medium spaced $d > 2a_c$ (figure 12) case.

these unlike-sign vorticity lobes in the vertical direction and become separated vertically with time. In addition to lobes separation, the emission of the TS wave reduces the strength of dipoles thereby reducing their propagation. The relative observations of figures 18(*b*) and 19(*b*) clearly reflect the abovementioned fact.

https://doi.org/10.1017/S0022377821000684 Published online by Cambridge University Press

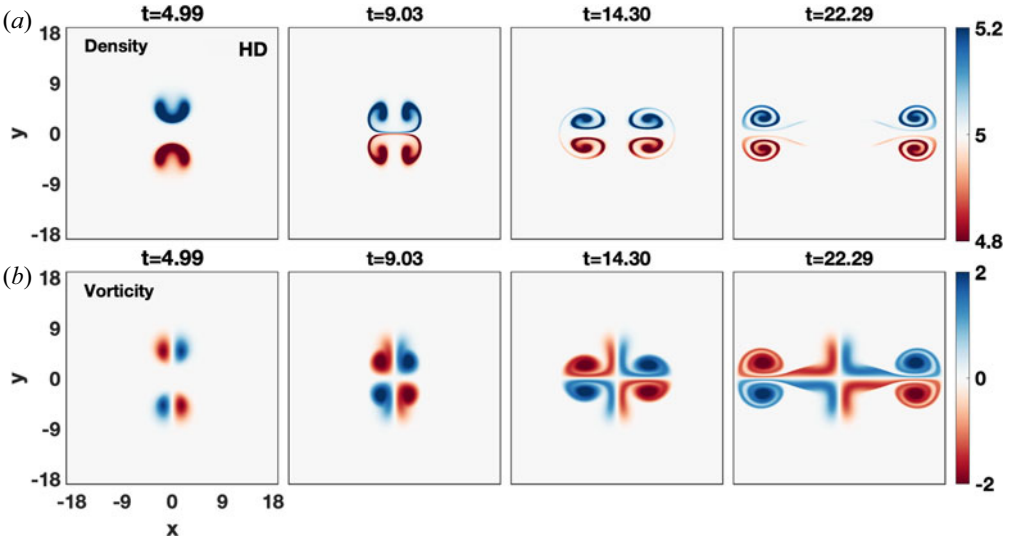

FIGURE 17. Time evolution of bubble–droplet density (*a*) and vorticity (*b*) for an inviscid fluid. Both are separated by distance $d = 12$ units ($d \gg 2a_c$, $a_c = 2$).

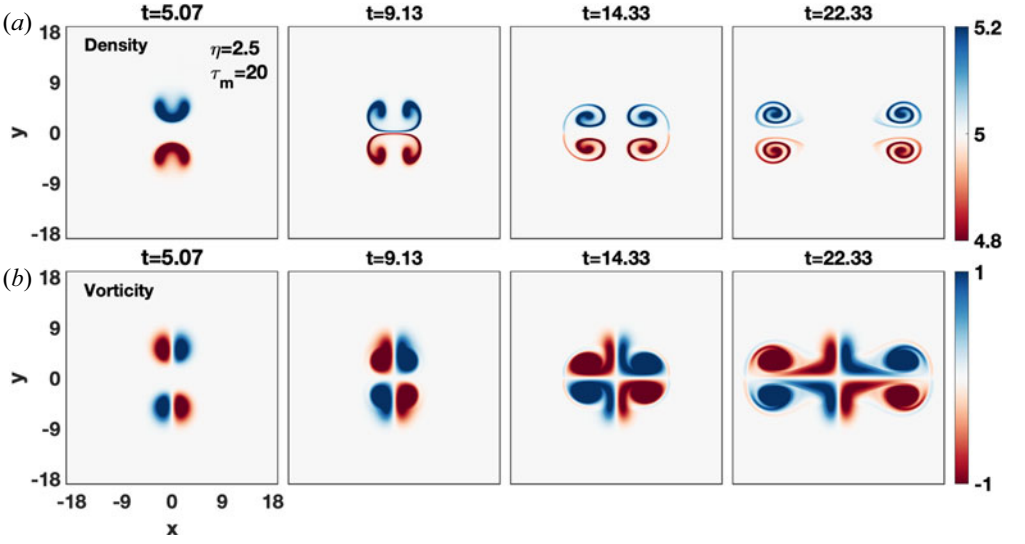

FIGURE 18. Time evolution of bubble–droplet density (*a*) and vorticity (*b*) for a viscoelastic fluid with $\eta = 2.5$ and $\tau_m = 20$.

Here, we restrict our study to this case only. However, other possible cases could be explored by varying the initial spacing. Furthermore, the collision between vertically aligned bubble and droplet with varying disparate strengths may lead to physical phenomena like interpenetration or a more complex trajectory after collision.

4. Summary and conclusion

In part I (Dharodi & Das 2021) of this investigation, in addition to the Rayleigh–Taylor instability, we simulated individual dynamics of a rising bubble and a falling droplet

https://doi.org/10.1017/S0022377821000684 Published online by Cambridge University Press

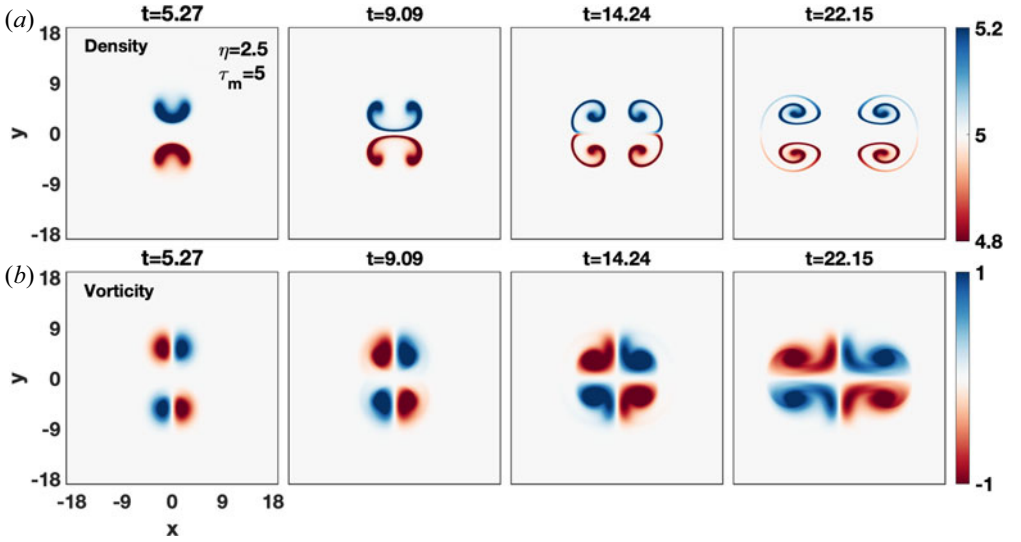

FIGURE 19. Time evolution of bubble–droplet density (a) and vorticity (b) for a viscoelastic fluid with $\eta = 2.5$ and $\tau_m = 5$.

in SCDP. We considered the SCDP as a viscoelastic fluid under the formalism of the generalized hydrodynamic fluid model. Here, with an interest to understand the interactions between a rising bubble and a falling droplet, we extend these individual dynamics to their combined evolution through two arrangements. A series of two-dimensional numerical simulations have been conducted.

In the first arrangement the bubble and droplet are manually placed side-by-side in a row together at the same height for three different initial spacings: widely spaced ($d \gg 2a_c$), medium spaced ($d > 2a_c$), and closely spaced ($d \approx 2a_c$), where a_c is core radius. To demonstrate how the appearance of τ_m controls the viscous spreading of the vorticity lobes, for each case, the coupling strength has been introduced as the mild-strong ($\eta = 2.5$, $\tau_m = 20$), medium-strong ($\eta = 2.5$, $\tau_m = 10$) and strong or strongest ($\eta = 2.5$, $\tau_m = 5$), as well as pure viscosity ($\eta = 2.5$, $\tau_m = 0$). It is observed that the net dynamics is governed by the competition between the side-by-side attraction of two inner like-sign vorticity lobes, owing to the merging process, and the vertical motion of two dipolar vorticities, owing to gravity. In the case of widely spaced, the forward vertical motion of dipolar vorticities dominates over the side-by-side attraction for the mild- and medium-strong coupling, while for the strong coupling case the mutual attraction of vorticity lobes dominates which results in a rotating tripolar structure. For the medium spaced case, a rotating tripolar structure is found for all the three coupling parameters. The reduction in the size of these structures is observed with increasing coupling strength. However, for an inviscid fluid the forward vertical motion of dipolar vorticities is observed. For the closely spaced case, the whole structure rotates for all the cases including the inviscid fluid. In the second arrangement, the droplet is placed above the bubble in a vertical column with fixed initial spacing. Here, in contrast to the previous case, there is no rotation of the bubble and droplet. Under the influence of gravity, the crescent-shaped bubble and droplet hit each other and their blobs become separated. One blob from the bubble and one blob from the droplet get paired with each other and subsequently move horizontally. We observe that their horizontal movement becomes slower with increasing the coupling strength of the medium.

https://doi.org/10.1017/S0022377821000684 Published online by Cambridge University Press

It would be interesting to observe the homo-interactions between a pair of bubbles rising or droplets falling side-by-side in homogeneous and heterogeneous background density media. In a heterogeneous medium, the dynamics would be more complex as the shear waves move slower in the denser side and faster in the lighter side (Dharodi 2020). Furthermore, the collisional interactions between the vertically aligned bubble and droplet of varying disparate strengths could be interesting, which may lead to the interpenetration or more complex trajectory after collision.

Supplementary material and movies

Supplementary material and movies are available at https://doi.org/10.1017/S0022377821000684. We include a movie to accompany the static images shown in figure 6. We also include the time evolution of vorticity profiles corresponding to the density profiles shown in figure 15(*a–c*).

Acknowledgements

The author thanks Bhawana for editing assistance. This research received no specific grant from any funding agency, commercial or not-for-profit sectors.

Editor Edward Thomas, Jr thanks the referees for their advice in evaluating this article.

Declaration of interest

The author reports no conflict of interest.

REFERENCES

ARZHANNIKOV, A.V., BATAEV, V.A., BATAEV, I.A., BURDAKOV, A.V., IVANOV, I.A., IVANTSIVSKY, M.V., KUKLIN, K.N., MEKLER, K.I., ROVENSKIKH, A.F., POLOSATKIN, S.V., *et al.* 2013 Surface modification and droplet formation of tungsten under hot plasma irradiation at the gol-3. *J. Nucl. Mater*. **438**, S677–S680.

BORIS, J.P., LANDSBERG, A.M., ORAN, E.S. & GARDNER, J.H. 1993 LCPFCT-A flux-corrected transport algorithm for solving generalized continuity equations. *Technical Report NRL Memorandum Report* 93-7192. Naval Research Laboratory.

CHANDRASEKHAR, S. 1981 *Hydrodynamic and Hydromagnetic Stability*. Dover, New York.

CHEN, R.-H., TAN, D.S., LIN, K.-C., CHOW, L.C., GRIFFIN, A.R. & RINI, D.P. 2008 Droplet and bubble dynamics in saturated fc-72 spray cooling on a smooth surface. *Trans. ASME J. Heat Transfer* **130** (10), 101501.

CHEN, Y.-H., CHU, H.-Y. & LIN, I. 2006 Interaction and fragmentatio of pulsed laser induced microbubbles in a narrow gap. *Phys. Rev. Lett*. **96** (3), 034505.

CHU, H.-Y., CHIU, Y.-K., CHAN, C.-L. & LIN, I. 2003 Observation of laser-pulse-induced traveling microbubbles in dusty plasma liquids. *Phys. Rev. Lett*. **90** (7), 075004.

CRISTINI, V. & TAN, Y.-C. 2004 Theory and numerical simulation of droplet dynamics in complex flows–a review. *Lab on a Chip* **4** (4), 257–264.

DHARODI, V.S. 2020 Rotating vortices in two-dimensional inhomogeneous strongly coupled dusty plasmas: shear and spiral density waves. *Phys. Rev.* E **102** (4), 043216.

DHARODI, V.S. & DAS, A. 2021 A numerical study of gravity-driven instability in strongly coupled dusty plasma. Part 1. Rayleigh–Taylor instability and buoyancy-driven instability. *J. Plasma Phys*. **87** (2), 905870216.

DHARODI, V.S., DAS, A., PATEL, B.G. & KAW, P.K. 2016 Sub-and super-luminar propagation of structures satisfying poynting-like theorem for incompressible generalized hydrodynamic fluid model depicting strongly coupled dusty plasma medium. *Phys. Plasmas* **23** (1), 013707.

DHARODI, V.S., TIWARI, S.K. & DAS, A. 2014 Visco-elastic fluid simulations of coherent structures in strongly coupled dusty plasma medium. *Phys. Plasmas* **21** (7), 073705.

DOLLET, B., MARMOTTANT, P. & GARBIN, V. 2019 Bubble dynamics in soft and biological matter. *Annu. Rev. Fluid Mech.* **51**, 331–355.

DWYER, H.A. 1989 Calculations of droplet dynamics in high temperature environments. *Prog. Energy Combust. Sci.* **15** (2), 131–158.

FRENKEL, J. 1955 *Kinetic Theory of Liquids*. Dover Publications.

GAUDRON, R., WARNEZ, M.T. & JOHNSEN, E. 2015 Bubble dynamics in a viscoelastic medium with nonlinear elasticity. *J. Fluid Mech.* **766**.

HUANG, M.-J. 2005 The physical mechanism of symmetric vortex merger: a new viewpoint. *Phys. Fluids* **17** (7), 074105.

JOSSERAND, C. & ROSSI, M. 2007 The merging of two co-rotating vortices: a numerical study. *Eur. J. Mech. (*B*/Fluids)* **26** (6), 779–794.

KAW, P.K. 2001 Collective modes in a strongly coupled dusty plasma. *Phys. Plasmas* **8** (5), 1870–1878.

KAW, P.K. & SEN, A. 1998 Low frequency modes in strongly coupled dusty plasmas. *Phys. Plasmas* **5** (10), 3552–3559.

KEVLAHAN, N.K.-R. & FARGE, M. 1997 Vorticity filaments in two-dimensional turbulence: creation, stability and effect. *J. Fluid Mech.* **346**, 49–76.

KONG, G., MIRSANDI, H., BUIST, K.A., PETERS, E.A.J.F., BALTUSSEN, M.W. & KUIPERS, J.A.M. 2019 Hydrodynamic interaction of bubbles rising side-by-side in viscous liquids. *Exp. Fluids* **60** (10), 1–15.

LEONG, F.Y. & LE, D.-V. 2020 Droplet dynamics on viscoelastic soft substrate: toward coalescence control. *Phys. Fluids* **32** (6), 062102.

LIU, J., MAK, T., ZHOU, Z. & XU, Z. 2002 Fundamental study of reactive oily-bubble flotation. *Minerals Engng* **15** (9), 667–676.

MEUNIER, P., LE DIZÈS, S. & LEWEKE, T. 2005 Physics of vortex merging. *C. R. Phys.* **6** (4-5), 431–450.

MOKHTARZADEH-DEHGHAN, M.R. & EL-SHIRBINI, A.A. 1985 Dynamics of two-phase bubble-droplets in immiscible liquids. *Wärme-Stoffübertrag.* **19** (1), 53–59.

NIEWIADOMSKI, M., NGUYEN, A.V., HUPKA, J., NALASKOWSKI, J. & MILLER, J.D. 2007 Air bubble and oil droplet interactions in centrifugal fields during air-sparged hydrocyclone flotation. *Intl J. Environ. Pollut.* **30** (2), 313–331.

NING, W., LAI, J., KRUSZELNICKI, J., FOSTER, J.E., DAI, D. & KUSHNER, M.J. 2021 Propagation of positive discharges in an air bubble having an embedded water droplet. *Plasma Sources Sci. Technol.* **30** (1), 015005.

RAYLEIGH, LORD 1900 Investigation of the character of the equilibrium of an incompressible heavyfluid of variable density. Scientific papers, pp. 200–207.

SCHWABE, M., RUBIN-ZUZIC, M., ZHDANOV, S., IVLEV, A.V., THOMAS, H.M. & MORFILL, G.E. 2009 Formation of bubbles, blobs, and surface cusps in complex plasmas. *Phys. Rev. Lett.* **102** (25), 255005.

SHEW, W.L. & PINTON, J.-F. 2006 Viscoelastic effects on the dynamics of a rising bubble. *J. Stat. Mech.: Theory Exp.* **2006** (01), P01009.

STENZEL, R.L. & URRUTIA, J.M. 2012 Oscillating plasma bubbles. I. Basic properties and instabilities. *Phys. Plasmas* **19** (8), 082105.

SWARZTRAUBER, P., SWEET, R. & ADAMS, J.C. 1999 Fishpack: efficient FORTRAN subprograms for the solution of elliptic partial differential equations. UCAR Publication.

TABOR, R.F., WU, C., LOCKIE, H., MANICA, R., CHAN, D.Y.C., GRIESER, F. & DAGASTINE, R.R. 2011 Homo-and hetero-interactions between air bubbles and oil droplets measured by atomic force microscopy. *Soft Matt.* **7** (19), 8977–8983.

TAYLOR, G.I. 1950 The instability of liquid surfaces when accelerated in a direction perpendicular to their planes. I. *Proc. R. Soc. Lond.* A. *Math. Phys. Sci.* **201** (1065), 192–196.

TENG, L.-W., TSAI, C.-Y., TSENG, Y.-P. & LIN, I. 2008 Micro dynamics of pulsed laser induced bubbles in dusty plasma liquids. In *AIP Conference Proceedings*, vol. 1041, pp. 333–334. American Institute of Physics.

VAN AKEN, G.A. 2001 Aeration of emulsions by whipping. *Colloids Surf.* A*: Physicochem. Engng Aspects* **190** (3), 333–354.

VAN HEIJST, G.J.F., KLOOSTERZIEL, R.C. & WILLIAMS, C.W.M. 1991 Formation of a tripolar vortex in a rotating fluid. *Phys. Fluids* A*: Fluid Dyn*. **3** (9), 2033–2033.

VON HARDENBERG, J., MCWILLIAMS, J.C., PROVENZALE, A., SHCHEPETKIN, A. & WEISS, J.B. 2000 Vortex merging in quasi-geostrophic flows. *J. Fluid Mech*. **412**, 331–353.

WANG, G.J., SHI, J.K., REINISCH, B.W., WANG, X. & WANG, Z. 2015 Ionospheric plasma bubbles observed concurrently by multi-instruments over low-latitude station Hainan. *J. Geophys. Res.: Space Phys*. **120** (3), 2288–2298.

XIE, L., SHI, C., CUI, X. & ZENG, H. 2017 Surface forces and interaction mechanisms of emulsion drops and gas bubbles in complex fluids. *Langmuir* **33** (16), 3911–3925.

ZHANG, J., CHEN, L. & NI, M.-J. 2019 Vortex interactions between a pair of bubbles rising side by side in ordinary viscous liquids. *Phys. Rev. Fluids* **4** (4), 043604.

ZHAO, L., BOUFADEL, M.C., KING, T., ROBINSON, B., GAO, F., SOCOLOFSKY, S.A. & LEE, K. 2017 Droplet and bubble formation of combined oil and gas releases in subsea blowouts. *Mar. Pollut. Bull*. **120** (1–2), 203–216.

ZHU, X., SUI, P.C. & DJILALI, N. 2008 Three-dimensional numerical simulations of water droplet dynamics in a PEMFC gas channel. *J. Power Sources* **181** (1), 101–115.

https://doi.org/10.1017/S0022377821000684 Published online by Cambridge University Press